ADVANCED ENERGY & SUSTAINABILITY RESEARCH
Open Access
www.advenergysustres.com

Ni Particle Morphology and Support Effect in the Catalytic Decomposition of Methane: Into the Design of Novel, High Yield Catalyst for Catalytic Decomposition of Methane

Jose A. Hernandez Gaitan, Xinyu Li, Kazuya Tamura, Koji Miyake, Yoshiaki Uchida, and Norikazu Nishiyama*

Research on high-surface-area supports and synergic promoters has been made, however, there is still much room for improvement on the catalytic-particles morphology and interaction with the support. A first approach for designing nanoplate supports to improve CDM catalysts was made. Amorphous aluminosilicates nanoplates (a-AS.np) with an average particle size of 23.4 nm and an average height of 2.8 nm, and α-Ni(OH)$_2$ nanoplates (Ni.np) with an average particle size of 23.2 nm and an average thickness of 8.4 nm, were successfully synthesized, using a two-dimensional reactor in amphiphilic phases (TRAP). Nickel loaded in a-AS materials with different morphologies and promotion effects of lantana (La^{3+}) & chromium (Cr^{3+}) species were studied. La-Cr promoted a-AS support showed an average increase of 13% on H_2 yield in severe conditions due to improved crystallization of Ni particles on mesoporous support and the electron promotion of La to Ni species. Furthermore, we evaluate the Ni.np as novel morphology support for La^{3+} & copper (Cu^{2+}) species in the methane decomposition reaction. La-Cu Ni.np showed outstanding performance and stability, a max H_2 yield of 15.9% (at 700 °C), and more than 400 min of H_2 generation (at 550 °C) compared to its a-AS support counterparts.

1. Introduction

Climate change is no longer a future problem, and the magnitude of the future consequences will depend on the total amount of greenhouse gases (GHG) we emit in our daily life activities and the effectiveness of our industrial processes today. Technology development, transfer and diffusion will play a key role to mitigate and even avoid some of the forecasted scenarios by successfully reducing GHG emissions.[1,2]

Fossil fuels are one of the main sources of GHG emissions and one of the most used in developing countries.[3] Alternative technological solutions, such as hydrogen energy systems, can become viable through intense research in production, storage, and usage. Currently, this alternative source development is starting to catch up, and the technological gaps are starting to close,[4–6] rapidly becoming a foreseeable alternative.

From the different actual methods to produce hydrogen: steam methane reforming (SMR),[7] dry methane reforming (DMR),[8–11] coal and biomass gasification,[12] electrolysis,[13,14] water splitting,[15,16] and autothermal processes;[17] SMR is frequently used due to its simplicity and efficiency, however, the SMR process generates large quantities of CO_2.[7]

An attractive alternative to this process is catalytic methane decomposition (CDM), which, in comparison, does not require a water-gas shift step and is a CO_x-free hydrogen process.

CDM shows great potential to obtain high methane conversion and hydrogen yield by using different supports for the metal catalyst. Currently, many challenges regarding the surface area and stability of the supported catalyst, the interaction between the metal catalyst and the support and the fine dispersion of the metal catalyst in the support, are yet to be improved.[18]

Several studies have been made to test the effectiveness of different metal-based catalysts for methane decomposition, and even when noble metals show outstanding catalytic activity, their use is restricted because of their low availability and their high cost. Ni-based catalysts have been proven to show the best catalytic performance for CDM reaction,[19–22] decreasing the

J. A. H. Gaitan, X. Li, K. Tamura, K. Miyake, Y. Uchida, N. Nishiyama
Division of Chemical Engineering
Graduate School of Engineering Science
Osaka University
1-3 Machikaneyama, Toyonaka, Osaka 560-8531, Japan
E-mail: k.miyake.es@osaka-u.ac.jp

K. Miyake, N. Nishiyama
Innovative Catalysis Science Division
Institute for Open and Transdisciplinary Research Initiatives (ICS-OTRI)
Osaka University
Suita, Osaka 565-0871, Japan

The ORCID identification number(s) for the author(s) of this article can be found under https://doi.org/10.1002/aesr.202400096.

DOI: 10.1002/aesr.202400096

thermal decomposition temperature from 1200 °C to temperatures between 500 and 600 °C. In addition, formations of carbon nanofibers and/or nanotubes at intermediate temperatures are attractive by-products for electrochemical applications.[23,24]

Hasnan et al. review the nature of catalyst support, preparation method, Ni metal loading on the support, and Ni modification by the addition of second and noble metal promoters for the methane decomposition reaction. Optimal catalysts depend on the nature of their support, their acidity, which promotes methane decomposition, as well as their surface area, morphology, and the proper interaction with the active metal, promoting the dispersion of the active phase and stabilizing the catalyst for improved resistance to sintering and coke formation.[25–28]

We evaluated the effect of amorphous aluminosilicates nanoplates (a-AS) with different morphologies as supports for NiO particles in CDM, the effect of metal promoters and furthermore the effect of α-$Ni(OH)_2$ nanoplates (Ni.np) both as active phase and support. a-AS.np and Ni.np were synthesized in between the layers of amphiphilic molecule (Brij L4) using a 2D reactor in amphiphilic phases (TRAPs),[29–31] and their catalytic performance was evaluated.

Additional promoters for a-AS samples were evaluated. Our laboratory has studied the effect of chromium III (Cr^{3+}) species in crystalline aluminosilicates in order to improve the acidity of the catalyst, decreasing coke formation in LDPE cracking and DMR.[8,32] Available literature on the effect of Cr species on CDM is scarce and inconclusive,[33,34] hence we decided to evaluate the effect of Cr^{3+} as a promoter for Ni/a-AS catalyst on its own and with a known metal promoter for CDM; lanthanum III (La^{3+}).[35,36]

Finally, we took advantage of the improved characteristics of Ni.np high surface area, micro/meso porosity and lamellar structure morphology, to use it as a support for well-known active metals for CDM: lanthanum and copper.[18,28,35,37,38]

2. Results and Discussion

In our laboratory we have synthesized a wide range of nanosheets and nanoplates materials using TRAPs.[29–31] In this research we tested both amorphous aluminosilicate sheets (a-AS.s) and Ni.np catalytic capabilities on CDM reactions.

2.1. Amorphous Aluminosilicate Support Characterization

Aluminosilicate-based supports including zeolites have shown a good synergic effect on CDM reactions,[8,27,37,39] showing high activities for hydrogen yield. Controlled a-AS.np morphology was evaluated as a support for Ni particles in CDM.

Three batches of a-AS were synthesized to evaluate their morphology effects on the surface area (S_{BET}) and support capabilities for Ni particles in CDM reaction as seen in **Table 1**: conventional a-AS synthesized in alkaline solution with reaction times of 0.5 and 2.0 h (a-AS.b and a-AS.m, respectively) and a-AS.s synthesized in TRAPs.

All a-AS samples X-Ray diffraction (XRD) patterns showed that samples were indeed amorphous as seen in Figure S1, Supporting Information, and Fourier transformed infrared (FT-IR) analysis confirmed the main functional groups of the aluminosilicate materials with characteristic Si–O–Si stretching band at 1063 cm^{-1} and different AlO species: Al_2O_3 (455.0 cm^{-1}), AlO_6 (780.0 cm^{-1}), and very small amounts of AlO_4 (561.0 cm^{-1}), as seen in Figure S6, Supporting Information (Table 1).

Table 1. Amorphous aluminosilicate supports samples.

Sample	$\overline{\varphi}_{IC/IA}$ [nm]	Si/Al molar ratio [−]	S_{BET} [$m^2\,g^{-1}$]
a-AS.b	60.0	45.5	18.3
a-AS.s	100.0	21.6	74.0
a-AS.m	45.0	14.4	180.6

Although a-AS samples have a similar plate-like primary structure, clear differences in their morphology and intra-crystalline/intra-agglomerate porous ($\overline{\varphi}_{IC/IA}$) size composition were observed by TEM and nitrogen adsorption analysis as seen in **Figure 1**. Both a-AS.b and a-AS.np samples showed $\overline{\varphi}_{IC/IA}$ macropores (60.0 and 100.0 nm, respectively) compared to $\overline{\varphi}_{IC/IA}$ mesopore of 45.0 nm for a-AS.m.

a-AS.b and a-AS.np main shape difference is attributed to the isotropic growth in between the HL phases of amphiphilic molecules; hence, we observed that a-AS.np presented disc-shape nanoplates. a-AS.np agglomerates range in lengths from 65.1 to 406.7 nm, with an average particle size of 215.5 nm and an average height of 2.8 nm. a-AS.b are bulky materials ($\overline{d} = 894.0$ nm) with less than 0.5 cm^3g^{-1} $\overline{\varphi}_{IC/IA}$ macropore volume.

Increased reaction time for a-AS.m showed that the same NaOH catalyst acted as an alkaline treatment for the formed a-AS hence we can observe a characteristic boomerang-like shape and a pear-like shape counterpart, due to the breakdown of the original plates. We mainly attribute the increased $\overline{\varphi}_{IC/IA}$ pore volume to this shape since it allows greater pore volume when stacked together compared to its plate counterparts as seen in Figure 1. The specific surface area (S_{BET}) for a-AS.b, a-AS.s, and a-AS.m supports were 18.3, 74.0, and 180.6 $m^2\,g^{-1}$, respectively.

First, we evaluated the effect of the a-AS morphology by loading 75.0% (w/w) nickel nitrate ($Ni(NO_3)_2{\cdot}6H_2O$) using a wet impregnation method, dried and calcined at 550 °C for 5 h to obtain Ni-based catalyst conformed of dispersed NiO on the a-AS surface. From this point on, we will refer to Ni-particles originated from bulk $Ni(NO_3)_2{\cdot}6H_2O$ as Ni.b.

Loading capacity (Ni/Si) for each support was observed by EDX, FE-SEM, and TPR analysis. **Table 2** shows that a-AS.b has the highest amount of nickel per gram of silica compared to other two samples. However, we can observe in **Figure 2** that a-AS.b loaded Ni-particles are bulky spheres with closed/closing powder morphology ($\overline{d} = 234.6$ nm), which has been found to encapsulate impurities, decrease the rate of nickel reduction, and wear out industrial equipment,[40] in agreement with TPR experimental data, where H_2 conversion was almost nonexistent, as seen in **Figure 3**.

a-AS.np didn't show a clear nickel morphology however, FE-SEM observation suggests that Ni-particles are in between a spherical open powder and aggregated crystals. Limiting the nucleation of nickel particles to flat surfaces promoted a vertical

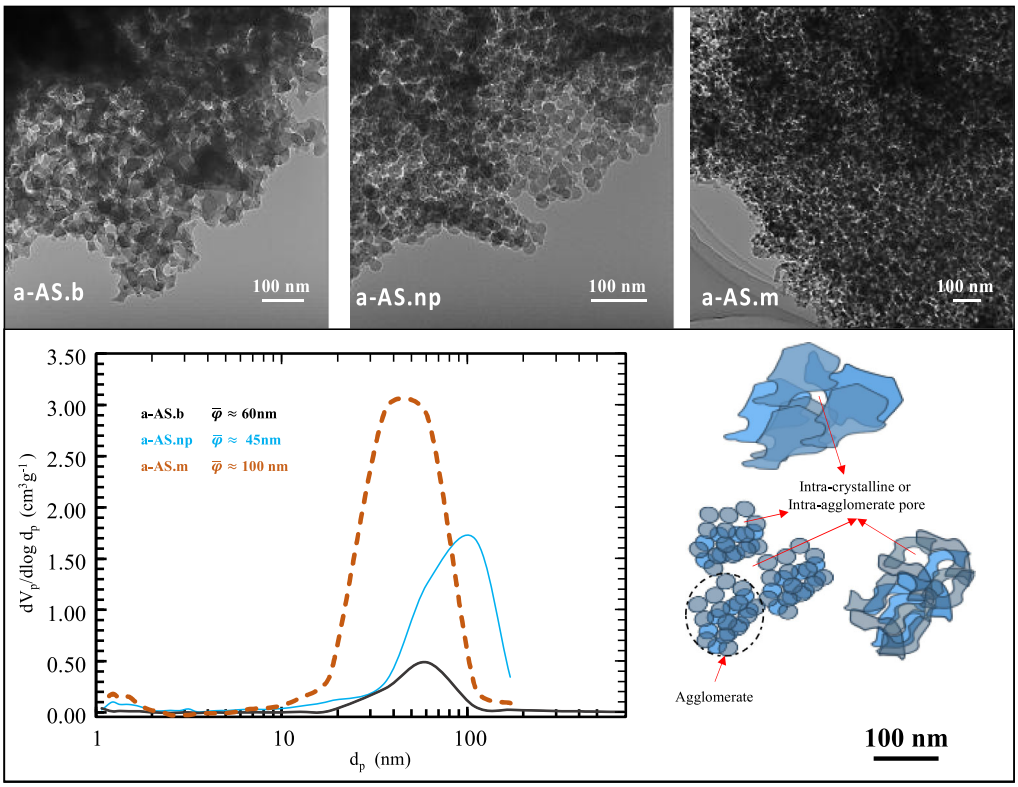

Figure 1. Morphology analysis based on STEM images and BJH plot of a-AS.b, a-AS.np and a-AS.m.

Table 2. Ni.b catalyst supported in a-as.

Sample	Si/Al molar ratio [–]	Ni/Si mass ratio [–]	S_{BET} [m^2g^{-1}]
Ni.b(75)/a-AS.b	6.2	1.8	9.5
Ni.b(75)/a-AS.np	9.4	1.1	11.9
Ni.b(75)/a-AS.m	8.9	0.8	73.6

agglomeration of Ni-particles and vertical growth. Available free Ni-particles promoted CDM reaction; however, it was hindered by the unfinished dispersion of Ni-particles.

Even when a-AS.m showed the lowest amount of Ni per gram of Si, TPR analysis showed the best CDM conversion. FE-SEM showed that Ni-particles were finely dispersed throughout the support and presented a truncated octahedron morphology. We concluded that porous materials with increased specific surface area promote the dispersion of Ni-particles throughout the support, avoiding agglomeration, reducing the size of the Ni-particles, and increasing their dispersion.

2.2. Metal-Supports Interactions

Based on the a-AS support results, we investigated the effect of metal promoters Cr and La on the Ni.b/a-AS.m catalysts. Due to the amount of sample required a new batch of mesoporous amorphous aluminosilicate was synthesized (a-AS.m_{ref}) with previously established conditions for a-AS.m synthesis.

a-AS.m_{ref} samples were doped with promoters (La and Cr) and active metal (Ni) in a two-step wet impregnation method. First, we added $La(NO_3)_3{\cdot}6H_2O$ or $Cr(NO_3)_3{\cdot}6H_2O$ to a-AS.m_2 at different concentrations via a wet impregnation method, then dried for 24 h and calcined at 550 °C for 5 h. Then 50% (w/w) $Ni(NO_3)_3{\cdot}6H_2O$ was added to the new promoted support via a wet impregnation method, dried for 24 h and calcined at 550 °C for 5 h. **Table 3** shows a summary of La and Cr samples analyzed. It was interesting to note that the amount of Ni loading was rather stable throughout the La and Cr series.

Chromium oxides have been reported as an effective promoter in diverse catalytic reactions due to their ability to protect the catalyst from sintering at high temperatures and their ability to avoid coke formation,[8,32,41] however, for a-AS.m supports, a decrease in H_2 yield in all combinations compared to unpromoted a-AS.m_{ref} was observed, as seen in **Figure 4**. FE-SEM showed high sintering at 550.0 °C with increased concentration of Cr and poor crystallization of Ni particles with no reaction at all for Ni.b(50)/Cr(19.7)a-AS.m_{ref}. This suggests strong interactions between Cr species and hydroxyl groups of a-AS,[32,41] and further strong interactions with Ni particles.

In contrast, lanthanum oxide has been reported to increase the dissociation rate of C—H bond by electron charge transfer to nickel,[35,38] and promote fine dispersion of nanocrystalline nickel particles in the lanthanum oxide matrix formed from the reduction of lanthanum nickel oxide.[36]

We could confirm by FE-SEM that in fact, nanocrystalline nickel particles were formed. H_2 yield was improved compared

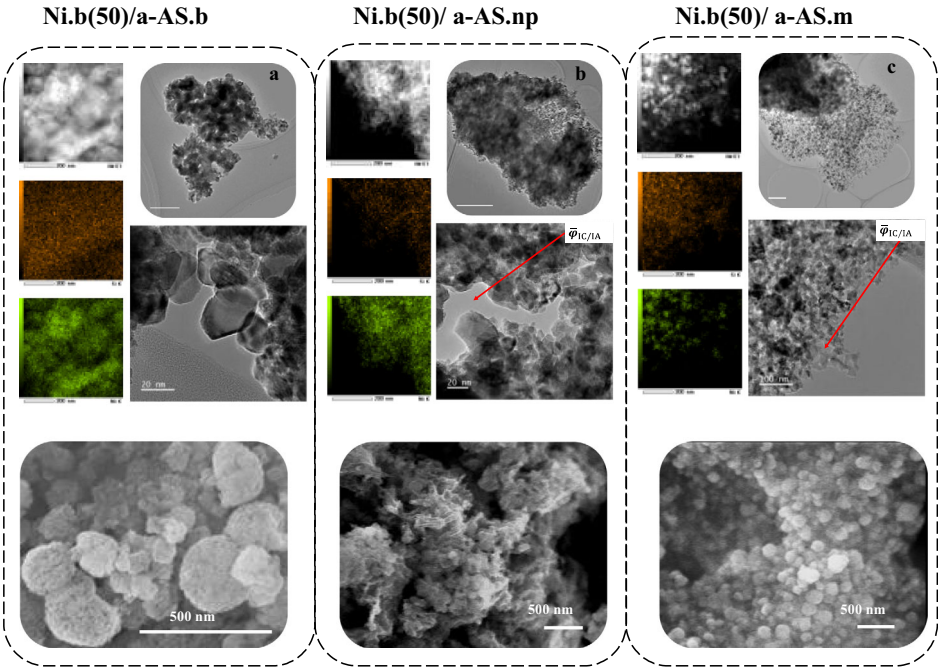

Figure 2. STEM/HAADF and FE-SEM of Ni.b loaded a-AS samples.

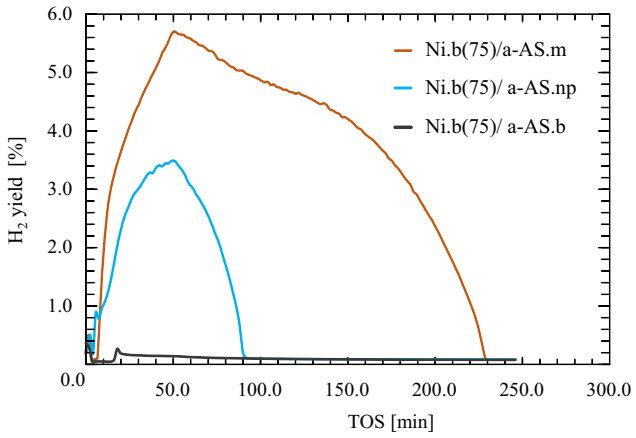

Figure 3. H_2 evolution on time for catalytic methane decomposition over Ni.b(75)/a-AS.m, Ni.b(75)/a-AS.np, and Ni.b(75)/a-AS.b at severe reaction conditions ($m_{cat} = 5.0$ mg, 20.0 sccm CH_4/5 sccm Ar, 550.0 °C).

to unpromoted a-AS.m_{ref}, starting from a concentration of 7.4% (w/w) of $La(NO_3)_3{\cdot}6H_2O$ in the support.

2.3. Ni-Particle Nanoplates

2.3.1. Ni.np Characterization

From the a-AS support studies, we established that the support morphology plays a crucial role in the Ni-particle morphology and catalytic performance. Hence, Ni-particle morphology was also studied.

Ni.np was synthesized using the TRAP method as described in the Experimental Section. Both XRD and FT-IR analysis showed that the synthesized Ni-nanoparticles were α-$Ni(OH)_2$, as seen in Figure S3 and S8, Supporting Information. Because of the broadening effect of nanoparticles, XRD pattern of α-$Ni(OH)_2$ showed limited peaks, however, characteristics (003), (006), (009), (101), and (110) peaks were observed.[42–47] Further confirmation was achieved by FT-IR analysis. α-$Ni(OH)_2$ characteristic vibrational bands 420, 460, and 612 cm^{-1} associated to the functional groups OH, NiO, and OH, respectively, were observed.[48–50] Additionally, α-$Ni(OH)_2$ has enlarged interlayer space allowing intercalation of water molecules, observed in the vibrational bands between 1200.0 and 1600.0 cm^{-1} as well as the increased vibrational band associated to hydrogen bonding observed in the vibrational band at 2320–2360 cm^{-1} due to increased trapped water.

Aggregated Ni sheets comprised of small nanoplates of 23.2 nm in diameter and an average height of 8.4 nm with a high surface area of 373.74 $m^2\,g^{-1}$ were synthesized in TRAPs. Aggregated porous nickel sheets showed an average size of 3700.0 × 2100.0 nm ($l \times w$) with an average thickness of 209.2 nm. Based on TEM analysis the self-assembly mechanism of lamellar nickel sheets resembles the growth mechanism proposed by Parvin and Cho for 3D flower-like $Ni(OH)_2$, but in our case, in 2D as seen in **Figure 5**.[48–50] Ni.np showed a predominant lamellar structure,[51,52] with low crystallization due to low temperature synthesis condition (T_{amb}) and the confining effects of the HL phases of TRAPs, restricting aggregation in the *y* axis.

Both Ni-particles obtained from the calcination of conventional $Ni(NO_3)_2{\cdot}6H_2O$ and α-$Ni(OH)_2$ were converted to NiO,[53] as seen in Figure S3, Supporting Information, where XRD patterns show the characteristic peaks of NiO compared to NiO

Table 3. Ni.b catalysts supported in a-as, promoted with La^{3+} and Cr^{3+} at different concentrations.

	Sample			Si/Al molar ratio [–]	Ni/Si mass [–]	La/Si mass ratio [–]	Cr/Si mass ratio [–]	S_{BET} [m^2g^{-1}]
Reference	Ni.b(50)	–	a-AS.m_{ref}	16.2	0.25	–	–	64.8
La-series	Ni.b(50)	–	La(3.8)a-AS.m_{ref}	6.0	0.58	0.04	–	53.3
	Ni.b(50)	–	La(5.2)a-AS.m_{ref}	8.4	0.53	0.06	–	51.5
	Ni.b(50)	–	La(8.2)a-AS.m_{ref}	7.7	0.66	0.09	–	60.0
	Ni.b(50)	–	La(20.9)a-AS.m_{ref}	7.2	0.61	0.26	–	62.3
Cr-series	Ni.b(50)	–	Cr(3.4)a-AS.m_{ref}	8.3	0.55	–	0.01	36.1
	Ni.b(50)	–	Cr(4.8)a-AS.m_{ref}	7.1	0.56	–	0.02	31.4
	Ni.b(50)	–	Cr(7.4)a-AS.m_{ref}	7.7	0.58	–	0.03	25.8
	Ni.b(50)	–	Cr(19.7)a-AS.m_{ref}	6.3	0.60	–	0.09	52.9

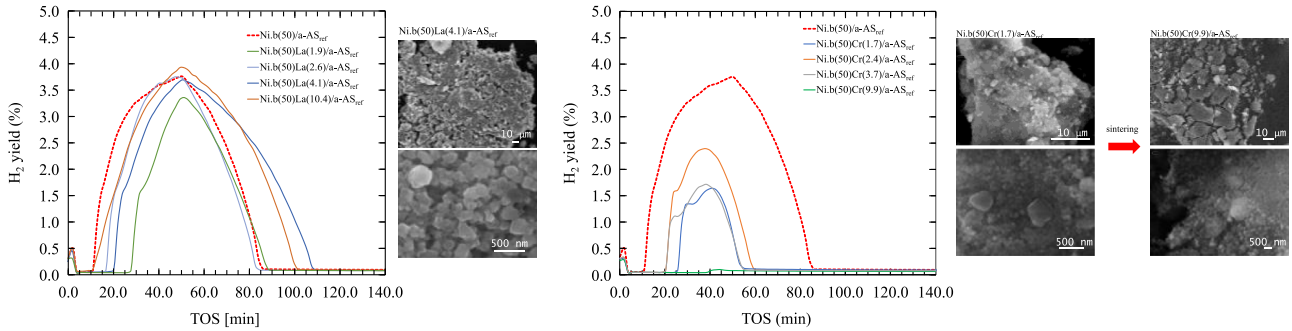

Figure 4. H_2 evolution on time for catalytic methane decomposition over Ni.b(50)/La(wt%)a-AS.m_{ref}, Ni.b(50)/Cr(wt%)a-AS.m_{ref} at severe reaction conditions (m_{cat} = 5.0 mg, 20 sccm CH_4/5 sccm Ar, 550 °C).

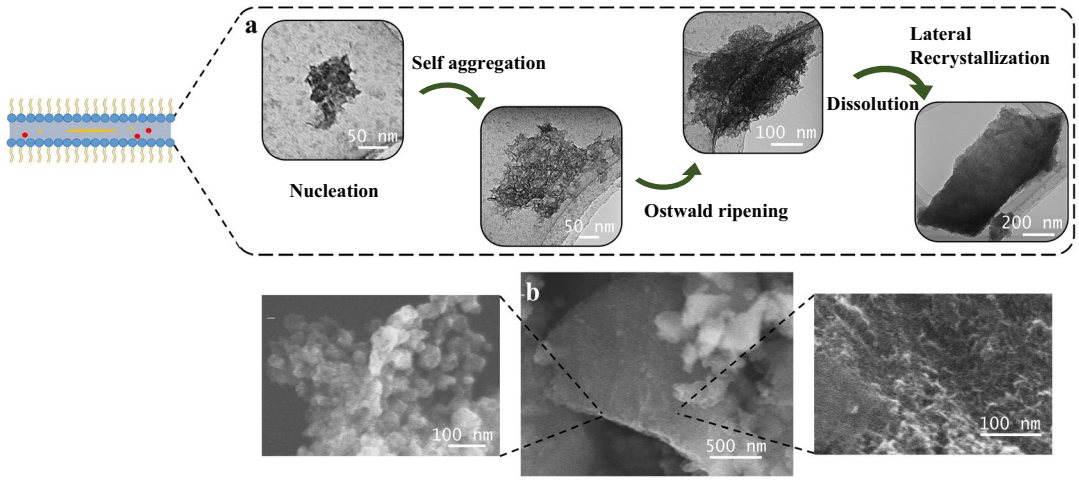

Figure 5. Proposed self-formation mechanism of Ni.np in TRAPs.

reference obtained from JADE 9 software. FT-IR also confirmed the conversion to NiO by the disappearance of the OH peaks as seen in Figure S8, Supporting Information.

Table 4 shows the specific surface area of Ni.np samples. High Ni.np S_{BET} was associated with the formation of a complex mixture of micro and mesoporous as seen in **Figure 6**. The displayed adsorption–desorption isotherm shows a mixture of Type I and Type IV isotherms in agreement with Barrett-Joyner-Halenda (BJH) plot analysis and a H2 type hysteresis loop suggesting the formation of inkbottle-shaped pores as seen in Figure S11, Supporting Information.

In order to activate the catalyst, a high temperature treatment (calcination) is required to reduce the catalyst, facilitating the crystallization of the nanoplate's unit cells, migrating from a

Table 4. Pure Ni samples.

Sample	S_{BET} [m^2g^{-1}]
$Ni(NO_3)_2{\cdot}6H_2O$	13.3
Ni.b (NiO)	7.8
Ni.np ($Ni(OH)_2$)	373.7
Ni.np-300 (NiO)	184.2
Ni.np-550 (NiO)	8.2

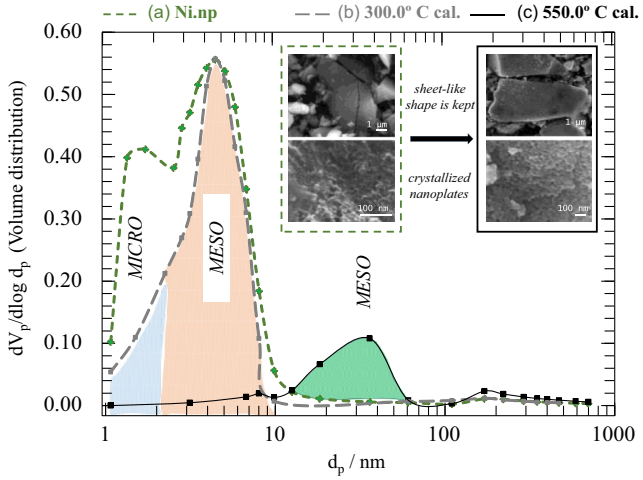

Figure 6. Pore size distribution of a) Ni.np (α-$Ni(OH)_2$), b) calcined Ni.np (NiO) at 300 °C, and c) calcined Ni.np (NiO) at 550 °C.

lamellar structure to defined crystals. As expected, the calcination temperature affects the crystallinity of Ni particles and it's reflected in the pore morphology. At 300 °C, only micropores disappear, but mesopores keep their size around 4.5 nm. However, when calcined at 550 °C, both previous micropores and mesopores disappear, and new mesopores with an average size of 35 nm are created suggesting that the degree of crystallization is correlated to the calcination temperature.

Most samples were calcined at 550 °C, hence, crystals are in between an octahedron and cubic crystal shape,[52] as seen in FE-SEM images. This crystal formation creates openings in the sheet-like structures forming mesoporous of 35 nm in diameter and resulting in the loss of micropores. This behavior is attributed to the conversion and crystallization of α-$Ni(OH)_2$ to NiO.

Since some of the first approaches to the adsorption of N_2 on pure and promoted nickel catalysts, it has been known that there is some degree of chemisorption on the nickel surface and that is very sensitive to the previous history of the catalyst.[54] These results are in agreement with previous studies on nickel catalysts, where specific surface area of improved Ni-catalysts decreases considerably when calcined and still the catalytic activity is improved as seen in **Figure 7**.[54,55]

2.3.2. Loading Capability of Ni.np

The loading capability of new synthesized Ni.np a-AS was also evaluated. First, we tested a wet impregnation method using ethanol and an ultrasound bath for 30 min to disperse the Ni.np, followed by the loading in a-AS.m, dried for 24 h and calcined at 550 °C. **Table 5** summarizes main characterization of loaded samples.

As seen in **Figure 8**, Ni.np/a-AS.m (ethanol) was not supported on a-AS.m and performed poorly at CDM. We concluded that Ni.np was not loaded onto the a-AS support. We tried a second method using an 8% HNO_3 solution (w/w) which solved the loading problem, but the Ni.np structure was decomposed. Although an improvement on the H_2 yield was seen when using dissolved Ni.np compared to Ni.b on a-AS.m, we cannot conclude that it was only because of the effect on the difference in size and morphology of dissolved Ni.b and Ni.np particles since the source of Ni was different and even when using the same ratio of Ni-source/support, Ni.np mass percentage of Ni is higher than Ni.b. Nonetheless, it was noteworthy to mention

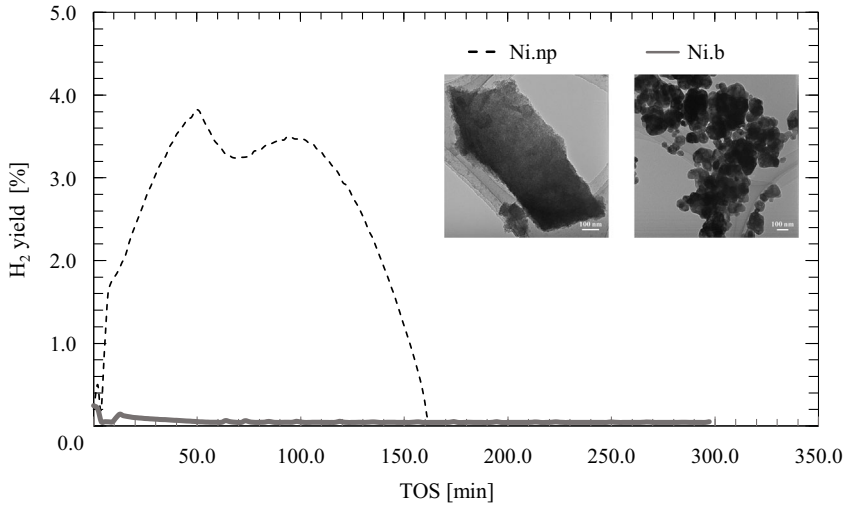

Figure 7. H_2 evolution on time for catalytic methane decomposition of pure Ni at severe reaction conditions (m_{cat} = 5.0 mg, 20 sccm CH_4/5 sccm Ar, 550 °C).

Table 5. EDX analysis and S_{BET} for the impregnation method effect on the loading of Ni-particles.

Sample			Wet-I_{method}	Si/Al molar ratio [–]	Ni/Si mass ratio [–]	S_{BET} [$m^2\ g^{-1}$]
Ni.b(75)	–	a-AS.m	$Ni(NO_3)_2{\cdot}6H_2O/H_2O$	8.88	0.8	73.6
Ni.np(75)	–	a-AS.m	Ni.np/ethanol	5.1	1.7	56.0
Ni.np(75)	–	a-AS.m	Ni.np/8% HNO_3	6.33	2.2	59.3

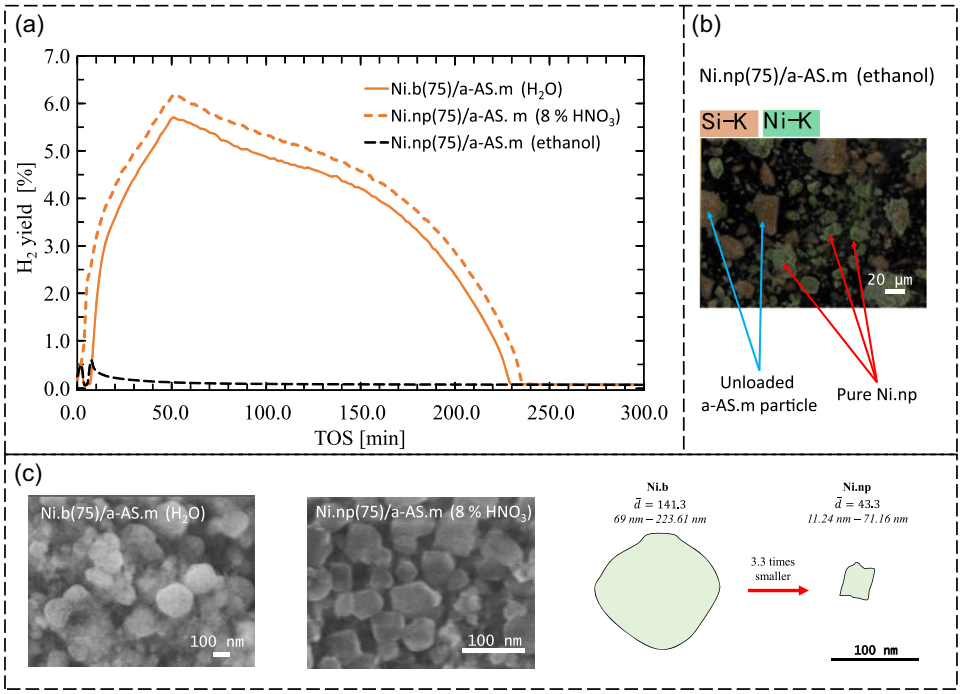

Figure 8. a) H_2 evolution on time for catalytic methane decomposition at severe reaction conditions (m_{cat} = 5.0 mg, 20 sccm CH_4/5 sccm Ar, 550 °C) of Ni.b and Ni.np over a-AS.m, b) MAP analysis of unloaded Ni.np on a-AS.m support, c) FE-SEM images of Ni.b and Ni.np particles loaded on the surface of a-AS.m support.

that Ni.np showed smaller particle size with truncated octahedral structures compared to bigger spherical Ni.b.

We found that the performance of Ni/a-AS catalyst cannot be determined based only on the amount of dispersed nickel in the final catalyst or the area of the catalyst, since other factors such as morphology of the unit cells, overall larger aggregates morphology and porous structure and the interactions between the active phase and support are key factors on the catalytic performance of CDM reaction as well.

2.3.3. Promoted a-AS on Dissolved Ni.np

We also evaluated the combined effect of La and Cr promoters in dissolving Ni.np. To do this, we decided to incorporate 0.7% (w/w) Cr_2O_3 and 1.4% (w/w) La_2O_3 during the polymerization step of TEOS and AIP for the synthesis of newly promoted a-AS to evaluate the impregnation effect of the promoters into the support. **Table 6** summarizes main characterization of La–Cr promoted samples.

Both Ni.np(75)/La(1.4)a-AS and Ni.np(75)/Cr(0.7)a-AS show similar behaviors to the Cr and La series from Section 2.2, decreasing the H_2 yield when promoting a-AS support. Even when Ni.np(75)/La(1.4)Cr(0.7)a-AS is the combination of the mass reactant's proportions for La_2O_3 and $Cr_2O_3{\cdot}9H_2O$, we observe a great increment in the amount of La loaded into the a-AS support, in agreement with the size increase of La particles in the La(1.4)Cr(0.7)a-AS compared to La(1.4)a-AS, from 39.2 nm in diameter to 103.6 nm when Cr species are added.

FT-IR showed the main vibrational bands of LaO, CrO, AlO, and SiO species, as seen in Figure S9, Supporting Information. Main attributes of SiO and AlO functional groups were maintained,[56,57] confirming the addition of metal-oxide species into the a-AS surface and framework, further confirmed by XRD analysis as seen in Figure S4, Supporting Information.

EDX showed the average composition of the different metals in the a-AS structure, where a considerable increment of La/Si and Cr/Si compared to the Cr and La samples from the study in Section 2.2 was observed, suggesting that metallic particles were also encapsulated by a-AS aggregates, limiting the metallic

Table 6. EDX analysis and S_{BET} for the la-cr promoted a-as samples, loaded with Ni.np by dissolution of 8% HNO_3.

Sample			Si/Al molar ratio [–]	Ni/Si mass ratio [–]	La/Si mass ratio [–]	Cr/Si mass ratio [–]	S_{BET} [$m^2 g^{-1}$]
Ni.np(75)	–	La(1.4)a-AS	4.9	2.9	0.12	–	55.7
Ni.np(75)	–	Cr(0.7)a-AS	2.5	3.0	–	0.35	88.2
Ni.np(75)	–	La(1.4) Cr(0.7)a-AS	1.1	5.6	0.61	0.26	84.6

promoters interaction with Ni-particles, which would also support the fact that Ni.np(75)/Cr(0.7)a-AS sampled didn't hindered H_2 generation as much as it was expected and Ni.np(75)/La(1.4)a-AS didn't improve it.

Furthermore, in La(1.4)Cr(0.7)a-AS, the 670 cm^{-1} vibrational band was not visible, possibly due to the absence of strong interactions of coordinated La^{3+} with 5- or 6- coordinated Al^{3+}, suggesting weak interactions between La_2O_3 and aluminosilicate. On the other hand, peaks derived from CrOH and CrO were clearly visible, suggesting favorable interactions with Cr_2O_3 and the aluminosilicate support.[57,58] Finally, the insertion of Cr species could have improved the interaction of La species with active species, hence overall H_2 yield of bimetallic La-Cr support was improved as seen in **Figure 9**.

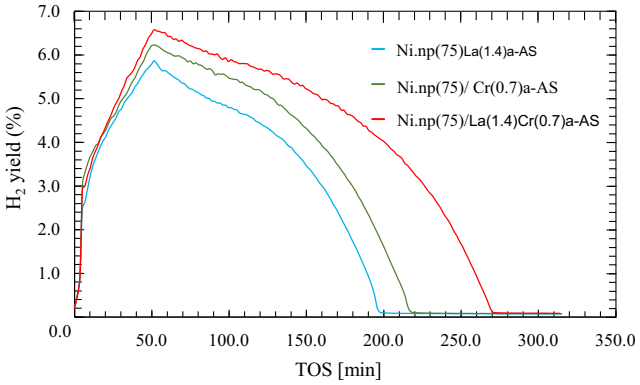

Figure 9. H_2 evolution on time for catalytic methane decomposition over Ni.np(75)/La(1.4)a-AS, Ni.np(75)/Cr(0.7)a-AS, and Ni.np(75)/La(1.4) Cr(0.7)a-AS at severe reaction conditions (m_{cat} = 5.0 mg, 20 sccm CH_4/ 5 sccm Ar, 550 °C).

XRD pattern of La(1.4)Cr(0.7)a-AS showed the characteristic peaks of a trigonal system of La_2O_3. In the case of Cr species, both CrO (560 cm^{-1}) and CrOH (620 cm^{-1}) vibrational frequencies were observed when adding Cr to the supports (Cr(0.7)a-AS and La(1.4)Cr(0.7)a-AS),[56] confirmed as well in the XRD patterns for Cr_2O_3.

Adsorption analysis showed that both a-AS.m and La(1.4)a-AS have a clear Type IV isotherm derived from mesoporous species, however, when using Cr species, the porous size decreases from 50 to 20 nm, approximately. Even when a Type IV isotherm is still predominant in Cr-supports, Figure S12c,d, Supporting Information, showed a significant reduction in the mesoporous size and availability due to the addition of crystal structures in the amorphous framework resulting in a constraining effect of the amorphous framework. **Figure 10** shows the pore volume distribution, showing that Cr has a positive effect by creating 18 nm mesoporous, which in the presence of lanthanum becomes beneficial for Ni loading and CDM.

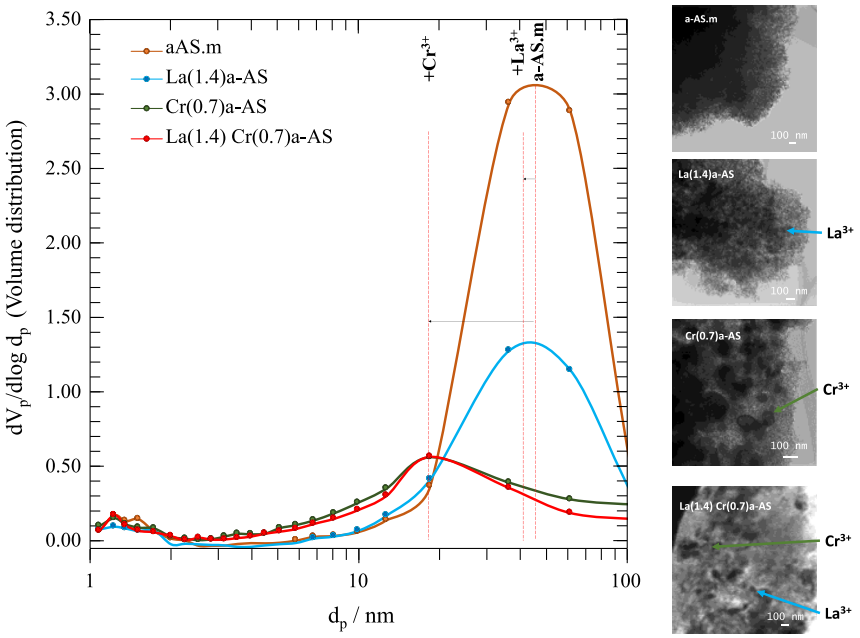

Figure 10. Porous size volume distribution behavior for La(1.4)a-AS, Cr(0.7)a-AS and La(1.4) Cr(0.7)a-AS (left), and TEM images of supports (right).

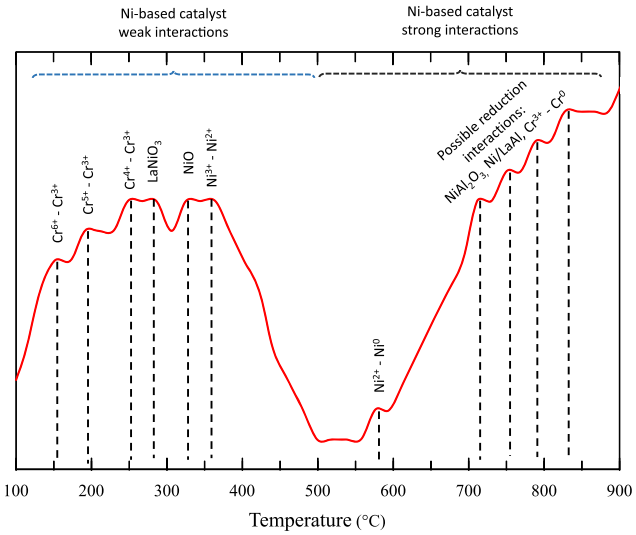

Figure 11. H_2 TPR analysis of Ni.np(75)/La(1.4)Cr(0.7)a-AS.

H_2-TPR profile of the bi-metallic promoter La(1.4)Cr(0.7)a-AS. As seen in **Figure 11**, several reduction bands were observed, due to the presence of La^{3+} and Cr^{3+} and their interaction with the support and the Ni-particles, clearly divided into two main areas; weak interactions from 150 to 400 °C and strong interactions from 700 to 1000 °C.

In the weak series, the first three peaks match different references for the Cr species reduction (Cr^{6+}, Cr^{5+} and Cr^{4+} to Cr^{3+}), next, the 286 °C peak might be allocated to weak interactions of Ni with La^{3+} followed by the reduction of Ni species (bulk NiO, Ni^{3+}–Ni^{2+} and Ni^{2+}–Ni^0) in agreement with several studies.[59–61] This region suggests that even at low temperatures, some CDM could still be achieved due to highly reactive chromium species that allow dehydrogenation. Potentially decreasing the overall required reaction temperature of the CDM.

In the strong interaction series, four peaks can be observed, attributed to strong interactions between Ni–La and Ni–Al and crystalline Cr_2O_3 (Cr^{3+}–Cr^0).[62–65] The strong interaction of Ni-particles with Al and La species improves the stability of the particles in the support. This strong interaction not only helps avoid sintering of the Ni-particles at the calcination step of the catalyst preparation but also extends the lifetime of the Ni-particles by preventing their detachment from the support when carbon nanotubes are forming.

2.3.4. Ni.np as Supports of Rare Earth/Transition Metals

Finally, Ni.np was evaluated as a support for known promoters of CDM: La and Cu metallic species.[28,36,38,59,66] La(50)Cu(12.5)/Ni.np catalyst was synthesized by the addition of $La(NO_3)_3{\cdot}6H_2O$ and $Cu(NO_3)_2{\cdot}3H_2O$ by wet impregnation method to Ni.np supports, dried for 24 h and calcined at 700 °C for 5 h. The presence of NiO, La_2O_3, and CuO was confirmed by XRD as seen in Figure S5, Supporting Information.

Figure 12 shows the morphology of the new La–Cu bimetallic catalyst supported in Ni.np.

Copper particles showed hexagonal nanodisc structures[67] leaving a hexagonal-shaped porous when aggregated. This aggregation pattern agrees with the transition from Ni.np cal mesoporous to the new catalyst macro porous of 65 nm diameter in average as seen in Figure S15, Supporting Information, and the aggregation pattern of metals over Ni.np sheets creating visible holes in the aggregated La–Cu particles. Lanthanum particles showed a spindle-like structure[68,69] and Ni particles had cubic-like structure.[52]

We tested this novel catalyst at 550 °C to compare it with previous samples, showing a huge improvement in stability at

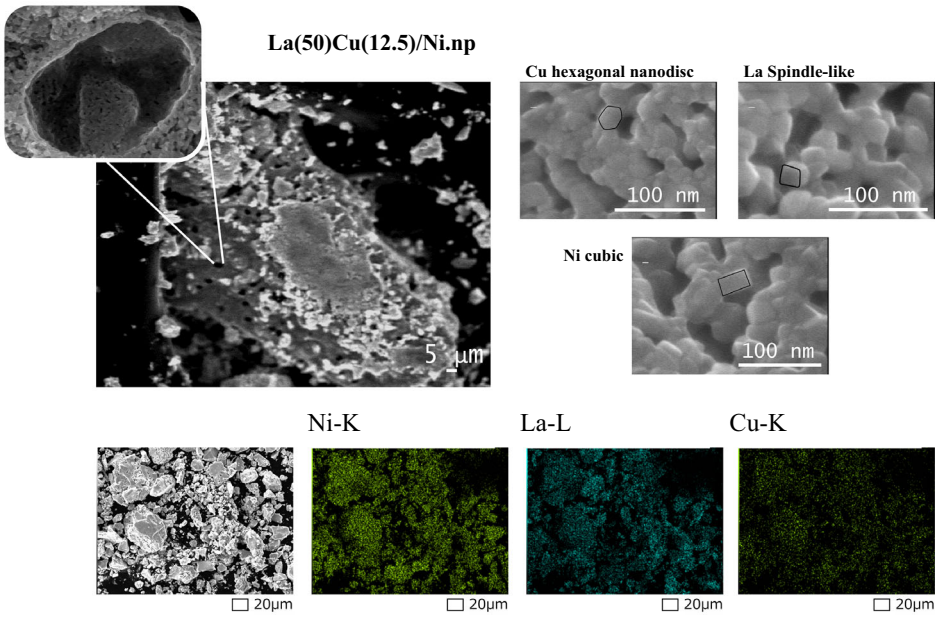

Figure 12. FE-SEM images and MAP analysis of La(50)Cu(12.5)/Ni.np.

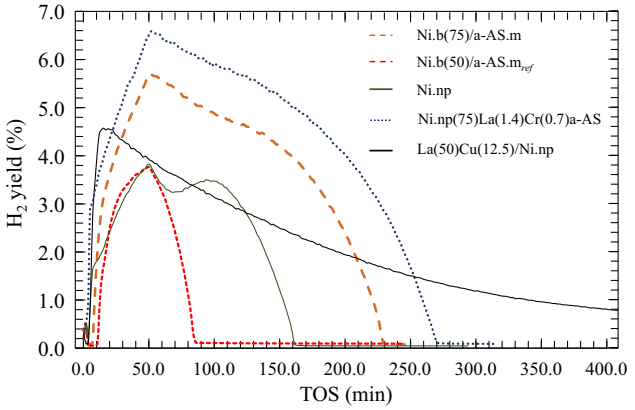

Figure 13. H_2 evolution on time for catalytic methane decomposition over La(50)Cu(12.5)/Ni.np at severe reaction conditions ($m_{cat} = 5.0$ mg, 20 sccm CH_4/5 sccm Ar, 550 °C).

severe conditions, more than 400 min. A general improvement in H_2 generation compared to pure Ni.b, Ni.np, all Ni(50) samples and improved stability compared to Ni(75) samples considering that La(50)Cu(12.5)/Ni.np uses less mass of Ni-source than all previous samples, as seen in **Figure 13**. We hypothesized that increased stability might be associated to the combination of different size C nanotubes created by the combination of hexagonal copper nanodisc particles and smaller octahedral nickel particles, creating gaps in between the nanotubes and avoiding aggregation and deactivation by carbon deposition, as seen in Image S1, Supporting Information.

We further examined the catalyst at an increased temperature of 700 °C and we observed an outstanding conversion of methane of 50.8% with H_2 yield of 15.9% at severe conditions. However, the deactivation at this temperature was around 80 min due to the increased deposition of carbon over the active sites.

Finally, **Figure 14** shows the La(50)Cu(12.5)/Ni.np catalyst analysis by NH_3 TPD, CO_2 TPD, and H_2 TPR, of this catalyst. NH_3 TPD profile didn't show any peaks, hence no acid sites were detected. CO_2 TPD showed two peaks at 140 and 680 °C indicating that the catalyst has basic properties. Finally, H_2 TPR showed three main peaks. The first peak (around 100–300 °C) corresponds to Cu reductions and interactions with Ni, weak interactions between La–Ni ($LaNiO_3$) and reduction of NiO and Ni^{3+}–Ni^{2+} takes place. Around 500 °C we have a clearly defined peak which is the main peak for Ni species reduction and finally, the last peak (starting around 650 °C) shows a stable activity up to 900 °C for strong interactions between Ni–La species and reduction of La species in agreement with La oxide's electron transfer capabilities.[35]

3. Conclusions

We successfully synthesized a novel Ni-based catalyst through a soft-template method, TRAP, with great implications in the future design of CDM catalysts. With this method, not only the support morphology and size of the support can be controlled, but also better understanding of the relation between the support surface and crystallization of active species and promoters was achieved. This has great implications for the design of future supported catalysts since both the support and active catalytic species can be tailored to different applications.

In agreement with previous studies, lanthanum species improved Ni dispersion and C—H dissociation by electron transfer to nickel for both a-AS (above 7.4% w/w) and Ni.np supports. Chromium, in contrast, showed detrimental effects for CDM as a-AS promoter. La promoters showed synergistic effects with Cr, improving the formation of mesoporous in the catalyst and the fine crystallization of Ni nanoparticles throughout a-AS supports.

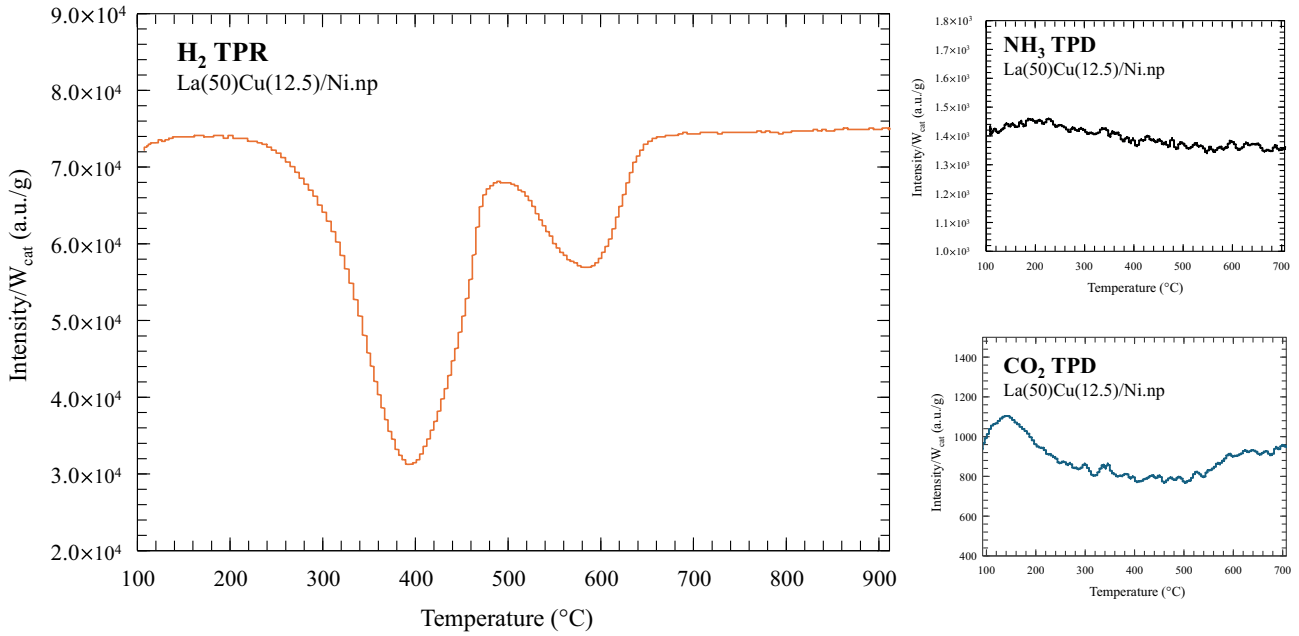

Figure 14. Full catalyst characterization (H_2 TPR – NH_3 TPD – CO_2 TPD) analysis of La(50)Cu(12.5)/Ni.np.

Porous Ni.np comprised of nanoplates of 23.2 nm in diameter and 8.4 nm in thickness were successfully synthesized using TRAPs, and further used as support for La and Cu promoters to improve their overall catalytic performance and stability. Max H_2 yield of 15.9% and more than 400 min of generation at severe conditions ($m_{cat} = 5.0$ mg, 20 sccm CH_4/5 sccm Ar, 550 °C)

Novel bi-metallic catalysts supported in Ni.np showed promising stability and conversion capabilities. Moreover, the TRAP method has unlimited potential to synthesize any type of metallic support from its nitrated form, enabling a wide range of supports for different combinations of catalysts and promoters.

4. Experimental Section

Materials: Tetraethylorthosilicate (TEOS, Wako Pure Chemicals Co.), aluminum isopropoxide (AIP, Nicalai Tesque Inc.), sodium hydroxide (NaOH, Wako Pure Chemicals Co.), nickel(III) nitrate hexahydrate (Wako Pure Chemical Co.), lanthanum(III) nitrate hexahydrate (Wako Pure Chemicals Co.), chromium(III) nitrate hexahydrate (Sigma-Aldrich Co.), chromium(III) oxide nonahydrate (Sigma-Aldrich Co.), copper (II) nitrate trihydrate (Sigma-Aldrich Co.), polyethylene glycol decyl ether (Brij L4, Sigma-Aldrich Co.), methanol (Wako Pure Chemicals Co.), heptane (Wako Pure Chemicals Co.) and deionized water were used without further purification to prepare the different supports and Ni-nanoparticles.

Preparation of Amorphous Aluminosilicate Synthesis: a-AS.b and a-AS.m samples were synthesized in an aqueous solution of TEOS as the source of silicon (16.2 wt%), AIP as the source of aluminum (0.3 wt%) and NaOH as a catalyst (0.6 wt%), agitated at 200 rpm and room temperature. a-AS.b and a-AS.m reaction time was 0.5 and 2 h, respectively. The final products were centrifuged at 11 000 rpm for 10 min, washed three times with ethanol and dried at 90 °C for 24 h.

TRAP was used to synthesize a-ASnp. The reaction takes place in the aqueous HL phases of the heptane solution. Composition of TRAP was Brij L4 (6.8 wt%), methanol (1.0 wt%), water (1.8 wt%), TEOS as the source of silicon (0.4 wt%), AIP as the source of aluminum (3.1×10^{-3} wt%) and NaOH as a catalyst (1.4×10^{-2} wt%), agitated at 200 rpm at 15 °C for 24 h. The final products were centrifuged at 11 000 rpm for 30 min and washed three times with ethanol and dried at 90 °C for 24 h.[30,31]

Preparation of Lanthanum Oxide: La_2O_3 was obtained by the calcination of $La(NO_3)_3{\cdot}6H_2O$ in air at 550 °C for 5 h.

Preparation of α-Ni(OH)$_2$ Nanoparticles: α-$Ni(OH)_2$ sheets were synthesized in the HL phases of the heptane solution of Brij L4 (10.7 wt%), methanol (0.7 wt%), water (3.3 wt%), $Ni(NO_3)_2{\cdot}6H_2O$ as the source of Ni (0.3 wt%) and NaOH as a catalyst (2.2×10^{-2} wt%), agitated at 200 rpm at room temperature for 24 h. The final products were centrifuged at 11 000 rpm for 30 min, washed three times with ethanol and dried at 90 °C for 24 h.

Impregnation of Ni-Particles: An impregnation process was performed referring to our previous works.[8,70,71] and modify accordingly to the needs of the different materials. Three types of wet impregnation methods were used for this study.

Impregnation of Ni-Particles: Ni(NO$_3$)$_2$·6H$_2$O: $Ni(NO_3)_2{\cdot}6H_2O$ was dissolved in water and put in an ultrasound bath for 30 min. Then the solution of $Ni(NO_3)_2$ was added to the support in a mortar and crushed together until we obtained a homogeneous mixture. The mixture was dried at 90 °C for 24 h and then calcined under air at 550 °C for 5 h. Ni-based catalyst obtained from commercial $Ni(NO_3)_2{\cdot}6H_2O$ are referred to as Ni.b/support. Depending on the analysis, 25:75 and 50:50 proportions were used for the loading of Ni.

Impregnation of Ni-Particles: α-Ni(OH)$_2$ Nanoparticles Loading: Since $Ni(OH)_2$ doesn´t dissolve in water, we tried two different approaches substituting the water from the previous impregnation method. α-$Ni(OH)_2$ nanoplates were dissolved in: 1) Dissolution in ethanol. 2) Dissolution in HNO_3 8% (w/w) solution.

The following procedure was exactly the same as the procedure above. After dissolution, α-$Ni(OH)_2$ solution was added into a mortar and crushed together with the support. The mixture was then dried at 90 °C for 24 h and finally calcined under air at 550 °C for 5 h. Ni-based catalysts obtained from commercial α-$Ni(OH)_2$ are referred to as Ni.np/support and samples obtained from novel sheets are referred to as Ni.np/support.

Preparation of Lanthanum and Chromium Series Samples: A series of La/Cr supports were synthesized using a two-step wet impregnation method.

In the first step, La or Cr were added to the a-AS via a wet-impregnation method. After at 90 °C for 24 h and calcined at 550 °C for 5 h, the promoted a-AS samples were loaded with 75% (w/w) Ni $(NO_3)_2{\cdot}6H_2O$, then dried at 90 °C for 24 h and finally calcined under air at 550 °C for 5 h.

For La samples, we used a mass range of 3.8–20.9%. (w/w) La:a-AS.m_{ref} and for chromium, a mass fight between 43.4 and 19.7 (w/w) Cr:a-AS.m_{ref}.

Preparation of La-Cr/a-as Supports: Three different metal-supports were synthesized using the following methodology.

La(1.4)a-AS was synthesized in an aqueous solution of TEOS (11.8 wt%), AIP (0.3 wt%), La_2O_3 (2.5×10^{-1} wt%), and NaOH (0.6 wt%).

Cr(0.7)a-AS was synthesized in an aqueous solution of TEOS (11.8 wt%), AIP (0.3 wt%), Cr_2O_3 (1.2×10^{-1} wt%), and NaOH (0.6 wt%).

La(1.4) Cr(0.7)a-AS was synthesized in an aqueous solution of TEOS (11.8 wt%), AIP (0.3 wt%), La_2O_3 (2.5×10^{-1} wt%), Cr_2O_3 (1.2×10^{-1} wt%), and NaOH (0.6 wt%).

All samples were agitated at 200 rpm and room temperature for 2 h. The final products were centrifuged at 11 000 rpm for 10 min, washed three times with ethanol and dried at 90 °C for 24 h.

Preparation of La(50)Cu(12.5)/Ni.Np Catalyst: 50% (w/w) $La(NO_3)_3{\cdot}6H_2O$ and 12.5% (w/w) $Cu(NO_3)_2{\cdot}3H_2O$ were dissolved in water and put in an ultrasound bath for 30 min. The solution was then added to Ni.np (α-$Ni(OH)_2$ nanoplates) support, previously placed in a mortar, and crushed together until we obtained a homogeneous mixture. The mixture was dried at 90 °C for 24 h and then calcined under air at 700 °C for 5 h.

Characterization: The chemical composition of the synthesized supports, Ni-particles and Ni-based catalyst was analyzed by scanning electron microscope-energy dispersive X-Ray spectroscopy (SEM-EDX) using a JEOL JCM-7000 microscope at 15 kV. The molecular structures of the synthesized materials were analyzed by Fourier-transform infrared (FT-IR) spectroscopy using a JASCO FT/IR–4600 with ATR PRO ONE single reflection accessory and XRD using a PANalytical X'Pert PRO diffractometer with Cu Kα radiation (45 kV and 40 mA).

XRD patterns were smoothened using and FTT filter by Origin2022 and compound reference patterns were generated using JADE 9 software. We observed the morphologies of the particles by transmission electron microscopy (TEM), obtained using a Hitachi H-800 at 200 kV. (N_2) adsorption was used to determine adsorption isotherms, specific surface area (S_{BET}) was calculated using BET method and porous analysis of the materials was obtained from BJH plot applied to the nitrogen adsorption isotherm using a BELSORPmax (MicrotracBEL).

Temperature program reduction (TPR) and desorption (TPD) analysis measurements were performed using BELCAT II equipped with a quadrupole mass spectrometer (MicrotracBEL).

Catalytic Decomposition of Methane (CDM) in Severe Experimental Conditions: All Ni-based catalysts were pelletized using a hydraulic press at 2 ton for 10 min. Then, the pellets were crushed and sieved using 300–850 micron sieves. The retained fraction was used for the CDM reaction. Harsh reaction conditions over Ni-based catalysts (5.0 mg) and under Ar flow at 550 °C were performed in a BELCAT II instrument (MicrotracBEL). The temperature program reduction consisted of a 2-step stabilization stage. First, temperature stabilized at 500 °C under Ar flow, followed by a reduction treatment of pure H_2 stream at the same temperature for 1 h. After the reduction treatment, residual H_2 is removed by Ar while adjusting the reaction temperature to 550 °C. Then, 80 vol% methane gas balanced by Ar was introduced into the reactor at a total flow rate of 25 sccm. H_2 produced during the CDM reaction was detected using a BELMASS instrument (MicrotracBEL). H_2 yield was calculated using a

calibration curve using inert Ar as a standard. The deposited carbon amount was analyzed by thermogravimetric analysis (TGA) using a DTG-60 (SHIMADZU), however, it was very difficult to obtain a homogeneous sample and a mass balance was performed instead using the mass gained after the reaction. The mass balance showed that there were no significant problems in our reaction experiments, as seen in Table S3, Supporting Information.

Supporting Information

Supporting Information is available from the Wiley Online Library or from the author.

Acknowledgements

A part of the present experiments was carried out by using a facility in the Research Center for Ultra-High Voltage Electron Microscopy, Osaka University. The authors would like to thank Dr. S. Takagi of the Research Center for Ultra-High Voltage Electron Microscopy, Osaka University, for assistance in the HTEM- HAADF-TEM observations.

Conflict of Interest

The authors declare no conflict of interest.

Data Availability Statement

The data that support the findings of this study are available from the corresponding author upon reasonable request.

Keywords

catalysis, hydrogen, methane, nano, particles

Received: March 22, 2024
Revised: May 15, 2024
Published online:

[1] Earth Science Communications Team, *Global Climate Change*, https://climate.nasa.gov/, (accessed: January 2024).
[2] Intergovernmental Panel on Climate Change (IPCC), *Climate Change 2021 – The Physical Science Basis: Working Group I Contribution to the Sixth Assessment Report of the Intergovernmental Panel on Climate Change*, Cambridge University Press, Cambridge, England **2023**.
[3] United Nations Environment Programme, *Emissions Gap Report 2022: The Closing Window - Climate Crisis Calls for Rapid Transformation of Societies*, Nairobi **2022**, https://www.unep.org/emissions-gap-report-2022 (accessed: January 2024).
[4] M. K. Singla, P. Nijhawan, A. S. Oberoi, *Environ. Sci. Pollut. Res.* **2021**, *28*, 15607.
[5] M. Yue, H. Lambert, E. Pahon, R. Roche, S. Jemei, D. Hissel, *Renew. Sustainable Energy Rev.* **2021**, *146*, 111180.
[6] A. Menéndez-Agudin, R. Rocca, G. Fernandez, L. Luengo-Baranguan, D. Zaldivar, *Renew. Energy Power Qual. J.* **2022**, *20*, 656.
[7] H. F. Abbas, W. M. A. Wan Daud, *Int. J. Hydrogen Energy* **2010**, *35*, 1160.
[8] K. Tamura, D. Murata, T. Sumi, S. Kokuryo, H. Kitamura, S. Tsubota, K. Miyake, Y. Uchida, M. Miyamoto, N. Nishiyama, *Energy Fuels* **2023**, *37*, 18945.
[9] T. Sumi, D. Murata, H. Kitamura, S. Kubota, K. Miyake, Y. Uchida, M. Miyamoto, N. Nishiyama, *Cryst. Growth Des.* **2023**, *23*, 3308.
[10] K. S. Nisa, V. Suendo, I. C. Sophiana, H. Susanto, A. Kusumaatmaja, N. Nishiyama, Y. W. Budhi, *Int. J. Hydrogen Energy* **2022**, *47*, 23201.
[11] I. C. Sophiana, F. Iskandar, H. Devianto, N. Nishiyama, Y. W. Budhi, *Nanomaterials* **2022**, *12*, 1556.
[12] A. Al Nashrey, *Eur. J. Energy Res.* **2022**, *2*, 8.
[13] S. Shiva Kumar, V. Himabindu, *Mater. Sci. Energy. Technol.* **2019**, *2*, 442.
[14] J. Brauns, T. Turek, *Processes* **2020**, *8*, 248.
[15] X. Tao, Y. Zhao, S. Wang, C. Li, R. Li, *Chem. Soc. Rev.* **2022**, *51*, 3561.
[16] Y. Ma, L. Lin, T. Takata, T. Hisatomi, K. Domen, *Phys. Chem. Chem. Phys.* **2023**, *25*, 6586.
[17] E. Matus, O. Sukhova, I. Ismagilov, M. Kerzhentsev, O. Stonkus, Z. Ismagilov, *Energies* **2021**, *14*, 5176.
[18] N. S. N. Hasnan, S. N. Timmiati, K. L. Lim, Z. Yaakob, N. H. N. Kamaruddin, L. P. Teh, *Mater. Renew. Sustain. Energy* **2020**, *9*, 8.
[19] K. Srilatha, D. Bhagawan, S. Shiva Kumar, V. Himabindu, S. Afr. *J. Chem. Eng.* **2017**, *24*, 156.
[20] F. Frusteri, G. Italiano, C. Espro, C. Cannilla, G. Bonura, *Int. J. Hydrogen Energy* **2012**, *37*, 16367.
[21] A. A. Ibrahim, A. H. Fakeeha, A. S. Al-Fatesh, A. E. Abasaeed, W. U. Khan, *Int. J. Hydrogen Energy* **2015**, *40*, 7593.
[22] N. Sánchez-Bastardo, R. Schlögl, H. Ruland, *Chem. Ing. Tech.* **2020**, *92*, 1596.
[23] T. Maneerung, K. Hidajat, S. Kawi, *Int. J. Hydrogen Energy* **2015**, *40*, 13399.
[24] R. Guil-Lopez, J. A. Botas, J. L. G. Fierro, D. P. Serrano, *Appl. Catal. A Gen.* **2011**, *396*, 40.
[25] V. Nichele, M. Signoretto, F. Menegazzo, A. Gallo, V. Dal Santo, G. Cruciani, G. Cerrato, *Appl. Catal.* **2012**, *111–112*, 225.
[26] O. Phichairatanaphong, P. Teepakakorn, Y. Poo-Arporn, M. Chareonpanich, W. Donphai, *Ind. Eng. Chem. Res.* **2021**, *60*, 4562.
[27] A. E. Awadallah, W. Ahmed, M. R. Noor El-Din, A. A. Aboul-Enein, *Appl. Surf. Sci.* **2013**, *287*, 415.
[28] A. Awad, M. A. Salam, D. V. N. Vo, B. Abdullah, *IOP Conf. Ser.: Mater. Sci. Eng.* **2020**, *5*, 11471.
[29] Y. Uchida, T. Nishizawa, T. Omiya, Y. Hirota, N. Nishiyama, *J. Am. Chem. Soc.* **2016**, *138*, 1103.
[30] K. Sasaki, J. A. Hernandez Gaitan, T. Okue, S. Matoba, Y. Tokuda, K. Miyake, Y. Uchida, N. Nishiyama, *Angew. Chem., Int. Ed.* **2022**, *61*, e202213773.
[31] J. A. Hernandez Gaitan, K. Sasaki, K. Miyake, Y. Uchida, N. Nishiyama, *Chem. Lett.* **2024**, *53*, upad034.
[32] S. Kokuryo, K. Tamura, K. Miyake, Y. Uchida, M. Miyamoto, Y. Oumi, A. Mizusawa, T. Kubo, N. Nishiyama, *Catal. Sci. Technol.* **2022**, *12*, 7270.
[33] A. E. Awadallah, A. A. Aboul-Enein, A. K. Aboul-Gheit, *Fuel* **2014**, *129*, 27.
[34] A. Rastegarpanah, M. Rezaei, F. Meshkani, K. Zhang, X. Zhao, W. Pei, Y. Liu, J. Deng, H. Arandiyan, H. Dai, *Appl. Catal. B* **2019**, *248*, 515.
[35] J. L. Figueiredo, J. J. M. Órfão, A. F. Cunha, *Int. J. Hydrogen Energy* **2010**, *35*, 9795.
[36] M. Pudukudy, Z. Yaakob, M. S. Takriff, *Energy Convers. Manage.* **2016**, *126*, 302.
[37] G. Urdiana, R. Valdez, G. Lastra, M.Á. Valenzuela, A. Olivas, *Mater. Lett.* **2018**, *217*, 9.
[38] A. F. Cunha, N. Mahata, J. J. M. Órfão, J. L. Figueiredo, *Energy Fuels* **2009**, *23*, 4047.
[39] A. E. Awadallah, D. S. El-Desouki, N. A. K. Aboul-Gheit, A. H. Ibrahim, A. K. Aboul-Gheit, *Int. J. Hydrogen Energy* **2016**, *41*, 16890.

[40] F. Ntuli, A. E. Lewis, *Chem. Eng. Sci.* **2007**, *62*, 3756.
[41] Y. Fujimoto, T. Sumi, K. Miyake, Y. Uchida, N. Nishiyama, *Chem. Lett.* **2022**, *51*, 515.
[42] Y. Qu, W. Zhou, X. Miao, Y. Li, L. Jiang, K. Pan, G. Tian, Z. Ren, G. Wang, H. Fu, *Chem. Asian J.* **2013**, *8*, 3085.
[43] D. S. Hall, D. J. Lockwood, C. Bock, B. R. MacDougall, *Proc. R. Soc. Lond., Ser. A* **2015**, *471*, 20140792.
[44] R. Thimmasandra Narayan, R. Kalyanaraman, *Indian J. Mater. Sci.* **2015**, *2015*, 1.
[45] M. S. Vidhya, G. Ravi, R. Yuvakkumar, D. Velauthapillai, M. Thambidurai, C. Dang, B. Saravanakumar, *RSC Adv.* **2020**, *10*, 19410.
[46] I. R. M. Kottegoda, N. H. Idris, L. Lu, J. Z. Wang, H. K. Liu, *Electrochim. Acta* **2011**, *56*, 5815.
[47] H. Cui, J. Xue, W. Ren, M. Wang, *J. Nanopart. Res.* **2014**, *16*, 2601.
[48] N. Parveen, M. H. Cho, *Sci. Rep.* **2016**, *6*, 27318.
[49] X. Ge, C. D. Gu, Y. Lu, X. L. Wang, J. P. Tu, *J. Mater. Chem. A Mater.* **2013**, *1*, 13454.
[50] E. Kordouli, B. Pawelec, K. Bourikas, C. Kordulis, J. L. G. Fierro, A. Lycourghiotis, *Appl. Catal. B* **2018**, *229*, 139.
[51] B. Chen, Y. Zhong, G. Shen, F. Wang, Z. Liu, M. Chen, W. Yang, C. Zhang, X. He, *Nanomaterials* **2020**, *10*, 194.
[52] D. Huang, H. Liu, T. Li, Q. Niu, *J. Solgel Sci. Technol.* **2019**, *89*, 511.
[53] S. Sagadevan, J. Podder, *Int. J. Nanopart.* **2015**, *8*, 289.
[54] R. J. Kokes, P. H. Emmett, *J. Am. Chem. Soc.* **1958**, *80*, 2082.
[55] D. Wang, R. Xu, X. Wang, Y. Li, *Nanotechnology* **2006**, *17*, 979.
[56] H. Li, H. Zhang, M. Luo, Y. Dong, H. Xu, X. Cheng, Z. Cai, *Water Pract. Technol.* **2021**, *16*, 1410.
[57] D. Caputo, M. Casiello, A. Milella, W. Oberhauser, A. Maffezzoli, A. Nacci, C. Fusco, L. D'Accolti, *Catalysts* **2020**, *10*, 1170.
[58] T. Schaller, J. F. Stebbins, *J. Phys. Chem. B* **1998**, *102*, 10690.
[59] D. Rivero-Mendoza, J. Stanley, J. Scott, K. F. Aguey-Zinsou, *Catalysts* **2016**, *6*, 170.
[60] F. Ayari, M. Mhamdi, D. P. Debecker, E. M. Gaigneaux, J. Alvarez-Rodriguez, A. Guerrero-Ruiz, G. Delahay, A. Ghorbel, *J. Mol. Catal. A Chem.* **2011**, *339*, 8.
[61] G. Tang, D. Gong, H. Liu, L. Wang, *Catalysts* **2019**, *9*, 442.
[62] Z. Xie, Y. Ren, J. Li, Z. Zhao, B. Liu, W. Song, L. Kong, X. Xiao, J. Liu, G. Jiang, *J. Catal.* **2019**, *372*, 206.
[63] T. Zhu, H. Song, F. Li, Y. Chen, *Catalysts* **2020**, *10*, 274.
[64] K. N. Papageridis, N. D. Charisiou, S. Douvartzides, V. Sebastian, S. J. Hinder, M. A. Baker, A. A. AlKhoori, S. I. AlKhoori, K. Polychronopoulou, M. A. Goula, *RSC Adv.* **2021**, *11*, 8569.
[65] T. A. Le, T. W. Kim, S. H. Lee, E. D. Park, *Korean J. Chem. Eng.* **2017**, *34*, 3085.
[66] W. X. Zhang, Y. Liang, J. W. Luo, A. P. Jia, Y. J. Wang, J. Q. Lu, M. F. Luo, *J. Mater. Sci.* **2016**, *51*, 6488.
[67] J. Dufour, C. Martos, A. Ruiz, M. Maroño, J. M. Sánchez, *Int. J. Hydrogen Energy* **2014**, *39*, 17600.
[68] E. L. Meyer, Mbese, Agoro, *Molecules* **2019**, *24*, 4223.
[69] J. Liu, G. Wang, L. Lu, Y. Guo, L. Yang, *RSC Adv.* **2017**, *7*, 40965.
[70] S. Karthikeyan, M. Parthibayarman, M. K. A. Mohammed, S. H. Mohammed, M. Selvapandivan, V. T. Srisuvetha. *Chem. Afr.* **2022**, *5*, 1427.
[71] H. Kitamura, T. Sumi, S. Kubota, S. Kokuryo, K. Tamura, K. Miyake, Y. Uchida, M. Miyamoto, N. Nishiyama, *Appl. Catal. A Gen.* **2023**, *668*, 119429.